

LA-UR-23-30722

Accepted Manuscript

Solid, structured composite neutron detectors with high dynamic range capability

Wiggins, Brenden W.
Richards, Cameron Gregory
Mclean, Thomas Donaldson
Iliev, Metodi
Favalli, Andrea
Hehlen, Markus Peter

Provided by the author(s) and the Los Alamos National Laboratory (2024-12-02).

To be published in: Journal of Applied Physics

DOI to publisher's version: 10.1063/5.0220543

Permalink to record:







<https://permalink.lanl.gov/object/view?what=info:lanl-repo/lareport/LA-UR-23-30722>



Los Alamos National Laboratory, an affirmative action/equal opportunity employer, is operated by Triad National Security, LLC for the National Nuclear Security Administration of U.S. Department of Energy under contract 89233218CNA000001. By approving this article, the publisher recognizes that the U.S. Government retains nonexclusive, royalty-free license to publish or reproduce the published form of this contribution, or to allow others to do so, for U.S. Government purposes. Los Alamos National Laboratory requests that the publisher identify this article as work performed under the auspices of the U.S. Department of Energy. Los Alamos National Laboratory strongly supports academic freedom and a researcher's right to publish; as an institution, however, the Laboratory does not endorse the viewpoint of a publication or guarantee its technical correctness.

RESEARCH ARTICLE | OCTOBER 23 2024

Solid, structured composite neutron detectors with high dynamic range capability

Brenden W. Wiggins ; Cameron G. Richards ; Thomas D. Mclean ; Metodi Iliev ; Andrea Favalli ; Markus P. Hehlen 



J. Appl. Phys. 136, 163104 (2024)
<https://doi.org/10.1063/5.0220543>



Articles You May Be Interested In

Light propagation in a neutron detector based on ^6Li glass scintillator particles in an organic matrix

J. Appl. Phys. (September 2018)

Improved neutron-gamma discrimination for a ^6Li -glass neutron detector using digital signal analysis methods

Rev. Sci. Instrum. (January 2016)

Investigations of radiation damaged arranged scintillating particle composites

J. Appl. Phys. (November 2021)



Journal of Applied Physics

Special Topics Open for Submissions

[Learn More](#)

Solid, structured composite neutron detectors with high dynamic range capability

Cite as: J. Appl. Phys. **136**, 163104 (2024); doi: [10.1063/5.0220543](https://doi.org/10.1063/5.0220543)

Submitted: 26 May 2024 · Accepted: 7 October 2024 ·

Published Online: 23 October 2024



Brenden W. Wiggins,^{1,a)} Cameron G. Richards,¹ Thomas D. Mclean,¹ Metodi Iliev,¹ Andrea Favalli,^{1,2} and Markus P. Hehlen¹

AFFILIATIONS

¹Los Alamos National Laboratory, Los Alamos, P.O. Box 1663, Los Alamos, New Mexico 87545, USA

²European Commission, Joint Research Centre (JRC), I-21027 Ispra, Italy

^{a)}Author to whom correspondence should be addressed: bww@lanl.gov

ABSTRACT

Neutron detectors are essential across disciplines such as fundamental science, nuclear security, safeguards, and civilian applications. While ³He-filled gas proportional counters have long been revered for their efficacy in detecting thermal neutrons and praised for their efficiency, neutron/gamma discrimination, and stability, the scarcity of ³He has spurred a search for alternatives. Here, we explore a solid structured scintillating particle composite (SPC) consisting of ⁶Li-containing scintillating glass particles within an acrylic matrix as a neutron detector for high dynamic range applications. We show for the first time that an SPC neutron detector can boast an intrinsic detection efficiency of 0.261% for pure ²⁵²Cf fission neutrons and an overall neutron detection efficiency of $(0.546 \pm 0.003)\%$ at the Neutron Free-in-Air facility while being able to function in an intense gamma-ray environment. We also show that the SPC neutron detector supports fast neutron capture times and enables a dual-readout scheme that extends the detector dynamic range to high incident neutron fluxes. A scalable fabrication process allows for tailoring the SPC detector properties to the requirements of specific applications. Good agreement is found between the experimental results taken with a National Institute of Standards and Technology traceable ²⁵²Cf source and the coupled MCNP6 and optical-ray-tracing simulations.

© 2024 Author(s). All article content, except where otherwise noted, is licensed under a Creative Commons Attribution (CC BY) license (<https://creativecommons.org/licenses/by/4.0/>). <https://doi.org/10.1063/5.0220543>

I. INTRODUCTION

Recently, Favalli *et al.* have demonstrated that scintillating particle composite detectors can provide robust performance in high neutron flux environments and outlined the value of heterogeneous composite detectors.¹ For practical applications in nuclear security and safeguards, however, it is highly advantageous for the heterogeneous composite to be all-solid-state. In solid scintillating particle composites (SPCs), the effective mixing of neutron capture materials in moderating materials enables fast neutron capture times and high neutron capture efficiency.^{1,2} Previous work pursued two main approaches: (1) using a moderating material that can scintillate, providing the utility of neutron capture gating methods and pulse-shape discrimination (PSD) techniques to register neutron events,^{3–5} and (2) using a moderating material that does not scintillate, providing the utility to restrict luminous background contributions and enabling a simple pulse-height threshold to register neutron events.^{6–9} This study focuses on the latter approach.

There are three major challenges for operating SPCs in a high neutron flux environment: (1) the ubiquitous gamma-ray backgrounds present, (2) the susceptibility to radiation damage of the SPC, and (3) count rate limitations based on the readout electronics. In general, the main drawback of bulk solid-state neutron scintillators (e.g., Cs₂LiYCl₆:Ce³⁺ scintillator crystal) is their inherent gamma sensitivity, which makes it difficult to detect neutrons in the presence of intense gamma-ray backgrounds.¹⁰ While both neutron capture and gamma-ray events can produce scintillation light events in SPCs, the scintillating particle composite approach can use small (~1 mm³) scintillating particles (e.g., commercial GS20 glass) to facilitate the maximum energy deposition of charged products from the ⁶Li(n,α)³H nuclear reaction while restricting gamma-ray energy deposition.^{2,7} Regarding susceptibility to radiation damage, Wiggins *et al.* have recently shown that acrylic-based GS20 composites can perform in high radiation environments and demonstrated a novel wavelength-shifting approach

18 November 2024 17:43:29

to reduce the scintillation light loss effects associated with radiation damage.¹¹ While digital processing methods, such as pulse-shape discrimination (PSD), can improve the gamma rejection ratio, the upper limit of the dynamic range in the pulse-counting mode is constrained by the inverse of the coincidence gate time requirements of the instrument; this limitation is further complicated by the gamma-ray background.¹² New approaches are needed to enable neutron detector systems (i.e., detector and readout electronics) that operate effectively within a high neutron flux environment; this is particularly significant in pulsed neutron applications where high neutron peak fluxes are expected.¹³

At the detector level, SPCs offer a tunable platform capable of modifying the interaction rate through the arrangement of scintillating particles. SPCs benefit from three critical features: (1) efficient neutron detection is accomplished by moderating incident neutrons to increase the probability of neutron capture on a $<50 \mu\text{s}$ timescale, (2) neutron capture events can generate localized energy deposition within the scintillating particle, creating a distinguishable light emission event compared to low-energy deposition gamma-ray events ($<1 \text{ MeV}$), and (3) scintillation light transport can be modified through the optical medium to a photo-detector that can operate in either the counting mode or current mode. The counting mode refers to traditional pulse-height analysis that counts individual neutron capture events per unit time; however, this assumes that the neutron capture events are temporally resolved. If neutron capture events are not temporally resolved, then pulses “pile up,” resulting in neutron events being registered with an incorrect amplitude or going unrecorded, necessitating the implementation of dead time correction methods.² The current mode refers to measuring the induced electrical current output of the photodetector. One of the unique benefits of measuring neutron events in the current mode is the ability to extend into high event rate regimes where individual pulses overlap and cannot be temporally resolved; however, this benefit comes with the trade-off of losing the ability to discriminate between neutrons and gamma rays, as scintillation light from both interactions contributes to the detector photocurrent. While the current mode cannot discriminate between neutron and gamma-ray interactions within the detector, this concept can work well with materials designed to suppress gamma event contributions.

In this study, we present the design, fabrication, and characterization of an SPC neutron detector with a particular focus on high dynamic range applications. A combination of nuclear particle (MCNP6) and optical-ray-tracing (FRED) modeling is used to inform the design of the SPC and to predict the time to neutron capture, intrinsic neutron detection efficiency, the gamma rejection ratio, and the pulse-height distribution. The significance of air voids in the SPC is examined. A prototype SPC is fabricated, and the fabrication process is expected to be scalable to larger detector volumes with automated manufacturing methods. Various low-activity gamma-ray and neutron button sources are used to measure the respective pulse-height distributions and gamma rejection ratios, and a NIST-calibrated high flux ^{252}Cf source at LANL's Neutron Free-in-Air (NFIA) facility is used to measure the overall neutron detection efficiency and to demonstrate a cross-calibration method that enables detector operation in a high incident neutron flux regime.

II. EXPERIMENTAL DETAILS

A. Simulations

1. MCNP6 modeling

To guide the development of the composite design, the MCNP6 software, equipped with the ENDF VII library, was utilized to simulate neutron and gamma interactions in the SPCs.^{14,15} The MCNP6 model of the composite was generated by creating an alternating odd-even array of scintillating particles with a fixed vertical and horizontal pitch, and the array was then positioned in a cylindrically shaped organic matrix. Additionally, an optimal configuration with respect to the particle size and pitch was chosen from previous work;⁷ specifically, this composite incorporated $0.1 \times 0.1 \times 0.1 \text{ cm}^3$ GS20 scintillator cubes with a horizontal sub-lattice particle pitch of 0.6 cm and a vertical sub-lattice particle pitch of 0.6 cm . The simulations assumed all of the lithium in the GS20 scintillator to be isotopically enriched ^6Li , with all other elements in natural abundance. The alternating odd-even cube placement is illustrated in Fig. 1. The alternating odd-even configuration is repeated with a lattice convention, supported in MCNP6, until the desired cylinder length is achieved. The cylindrical composite

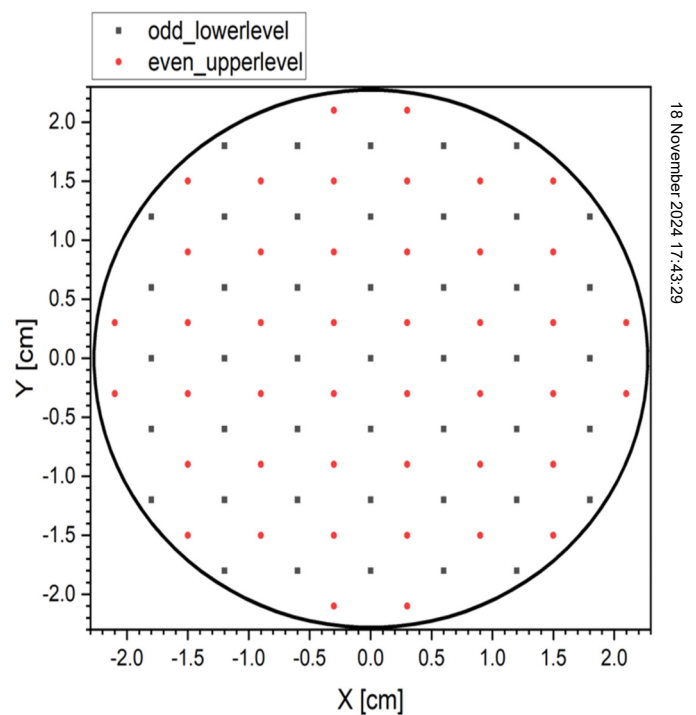


FIG. 1. Illustration of the odd-even scintillating cube configuration in the acrylic matrix; here, the alternating odd-even arrangement is demonstrated with different symbols. The black squares represent the odd lower-level arrangement, and the red circles represent the even upper-level arrangement. The solid line border serves as a guide to the eye. The odd-even configuration was used to enhance the volume fraction of the scintillating cubes while maximizing the inter-particle distances within the organic medium.

had dimensions of 4.6 cm diameter and 5.08 cm length. The spatial position and energy deposition of the ${}^6\text{Li}(n,\alpha){}^3\text{H}$ events or the gamma-induced electron interactions were acquired by post-processing the MCNP6 output files. The simulations used ${}^{252}\text{Cf}$ as a representative fission source, while ${}^{60}\text{Co}$ and ${}^{208}\text{Tl}$ sources were used to investigate the response characteristics of the composite at different gamma-ray energy ranges. The ${}^{60}\text{Co}$ source emits gammas with energies of 1.173 and 1.332 MeV, while the ${}^{208}\text{Tl}$ source emits a set of gamma rays up to 2.614 MeV. Notably, for the ${}^{208}\text{Tl}$ case, only the main emission of 2.614 MeV was considered. The gamma rejection ratio for incident gamma rays was determined by calculating the number of gamma energy deposition events arriving in the energy deposition range for a ${}^6\text{Li}(n,\alpha){}^3\text{H}$ event with the F8 tally; here, the ${}^6\text{Li}(n,\alpha){}^3\text{H}$ energy distribution was assumed as a Gaussian distribution with an average of 1.6 MeV electron equivalence and a full width at half maximum (FWHM) of 15% based on previous measurements.⁶ The incident ${}^{252}\text{Cf}$ fission neutron source was modeled as a Maxwell–Boltzmann distribution with a recommended neutron temperature of 1.42 MeV, while the fission gamma energy distribution was sampled from the ENDF library.¹⁴ The incident neutrons and gammas were configured to irradiate the cylindrical detector's lateral surface with the incidence angle varying with respect to the lateral surface normal vector. The neutron capture time was also investigated to determine the average time a neutron takes to be captured within the scintillating particle composite volume; here, the neutron capture time is defined as the absolute value of the difference between the time the neutron enters the composite volume and the time it is captured by the ${}^6\text{Li}(n,\alpha){}^3\text{H}$ interaction. The neutron capture time was explored with the F4 time-tally convention; here, triton tracks through the GS20 scintillating particle volume are compiled as a function of time with 0.1 μs time bins. The neutron capture times were extracted by performing a least squares fit of the function

$$y = y_0 + A_1 \exp\left(\frac{x_0 - x}{\tau_1}\right) + A_2 \exp\left(\frac{x_0 - x}{\tau_2}\right) + A_3 \exp\left(\frac{x_0 - x}{\tau_3}\right) \quad (1)$$

to the F4 tally result. Here, y_0 is the baseline offset, x_0 is the time offset, x is the time variable, τ_1 , τ_2 , and τ_3 are the decay constants, and A_1 , A_2 , and A_3 are the corresponding weights for each component. All MCNP6 simulations used 10^7 incident neutrons.

The NFIA capability was designed as a low neutron scatter facility for calibrating neutron instruments and dosimeters. It has been extensively modeled using MCNP6 for calculating the neutron fluence and dose rate as a function of distance from a suite of neutron sources, including the ${}^{252}\text{Cf}$ source of interest to this study. The comprehensive MCNP model relied on the data of the cross section from the ENDF/B-VII.1 nuclear data library, including the low-energy neutron treatment [i.e., $S(\alpha, \beta)$ tables] for neutron transport.^{14,15} Similar to the composite modeling effort, the ${}^{252}\text{Cf}$ source term was modeled as a Maxwell–Boltzmann distribution with the recommended neutron temperature of 1.42 MeV.¹⁶ Point detector tallies (F5 type) were used to calculate the total fluence per source neutron at several distances. These F5 fluence tally results were then scaled based on the NIST-traceable decay-corrected source emission rate for each day of the study.

2. Optical ray tracing and pulse-height spectra modeling

Optical-ray-tracing simulations, utilizing the FRED Optical Engineering Software (Photon Engineering, Tucson, AZ), investigated the transport of scintillation light in SPCs. Two distinct cases were explored: (1) a structured composite with no air voids and (2) a structured composite with air voids. To compare each case, the average light transport efficiency was calculated to explore the changes in optical transport. The light transport efficiency was defined as the ratio of the total optical power from photons reaching the planar end face of the cylindrical composite [where the photomultiplier tube (PMT) is attached] to the total optical power emitted in the scintillation event. The average light transport efficiency is determined by calculating the average of light transport efficiency values for individual GS20 particles along a common longitudinal position. Notably, the optical-ray-tracing simulations did not include an optical coupling medium between the composite and the PMT plane. The corresponding material optical properties were taken from the literature; here, additional optical-ray-tracing simulation details can be found in previous work.¹¹ Figure 2 illustrates the simulation cases explored in this work.

To create a histogram of generated photoelectrons per scintillating event, a representative spectrum that is similar to the pulse-height distribution, the number of photons created for a ${}^6\text{Li}(n,\alpha){}^3\text{H}$ nuclear reaction, and the number of photons arriving at the PMT optical face must be determined. Through the utilization of FRED, the



FIG. 2. Optical-ray-tracing simulation cases for a composite without air voids and for a composite with air voids. The color legend indicates the materials used for each case.

number of photons arriving at an optical face of the composite was calculated by taking the average light transport efficiency of scintillating particles along a common longitudinal position. The number of scintillation photons generated from the ${}^6\text{Li}(n,\alpha){}^3\text{H}$ nuclear reaction was assumed to be a Gaussian distribution with an average photon yield of 6000 photons per captured neutron and a measured standard deviation of 3.7%.¹¹ The light yield for energetic electrons was estimated to be 4343 photons/MeV; this value was approximated by the Compton edge generated by exposing $0.1 \times 0.1 \times 0.1 \text{ cm}^3$ GS20 scintillator cubes to 662 keV gamma rays from a ${}^{137}\text{Cs}$ source. The difference in light output from the ${}^6\text{Li}(n,\alpha){}^3\text{H}$ nuclear reaction compared to energetic electrons is primarily due to quenching effects.¹⁷

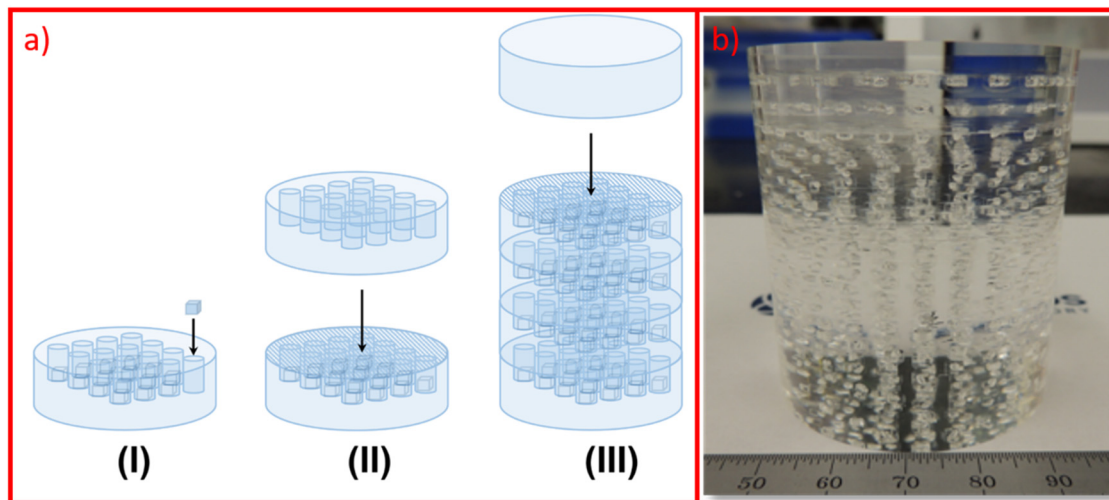
The estimated number of photoelectrons generated for each ${}^6\text{Li}(n,\alpha){}^3\text{H}$ nuclear reaction was determined by sampling the Gaussian function describing scintillation events for neutron capture, followed by multiplying the sampled quantity by the average light transport efficiency along a common longitudinal position and the PMT quantum efficiency. The photo-electron multiplication, for each dynode on the PMT, up to the seventh dynode, was modeled as a Poisson distribution with an average of four electrons created for each incident electron; here, the Poisson distribution was sampled for each incident electron. A list of electrons generated for each scintillation event [i.e., ${}^6\text{Li}(n,\alpha){}^3\text{H}$ or energetic electron interaction] was tabulated to then create a total photoelectrons generated histogram.

B. Multi-layer composite fabrication

To explore the feasibility of fabricating a solid, structured composite with an alternating odd-even configuration and compare the calculated characteristics to measured quantities, one representative

composite was fabricated for the experiments. To achieve the desired GS20 cube horizontal and vertical pitch, multiple blind holes were bored into 5 cm diameter \times 0.3175 cm thick UV transmitting (SUVT, Polymer Plastics, Carson City, Nevada) acrylic disks. The blind holes had a 0.14 cm depth with a 0.2 cm diameter. A total of 16 disks were fabricated, accommodating $0.1 \times 0.1 \times 0.1 \text{ cm}^3$ GS20 cubes under the constraint of one cube per hole. The cubes were constructed by cutting a monolithic $10 \times 10 \times 0.1 \text{ cm}^3$ GS20 plate (Scintacor, Cambridge, UK) into $0.1 \times 0.1 \times 0.1 \text{ cm}^3$ GS20 cubes with a precision diamond wheel saw (American Precision Dicing, Inc, San Jose, CA). Notably, a small variability is expected in the inter-particle pitch due to the blind-hole diameter. The range of variability is between 0.05 and 0.029 cm, depending on the cube's orientation within the hole.

Stacking of the disks occurred in an alternating order of solid disks with an odd layer and then an even layer, with a total of 17 disk layers. Figure 3(a) illustrates the assembly process. First, one surface of a solid disk was coated with a poly methyl methacrylate (PMMA)-based, UV-curable resin that was index-matched to UV transmitting acrylic. The resin contained a mixture of methyl methacrylate (MMA) and PMMA molecules with 2-hydroxy-2-methylpropiophenone (Sigma-Aldrich, Saint Louis, Missouri) as a UV photo-initiator. The resin used a 1:6 weight ratio of PMMA to MMA to control viscosity. Additionally, 10% of 2-hydroxyl-2-methylpropiophenone was added by weight (with respect to the PMMA/MMA mixture) and heated to approximately 40 °C until the polymer was completely dissolved to obtain the final resin product. Notably, GS20 cubes were inserted in each hole and forced to the bottom. Each hole was then backfilled with resin to account for the displaced volume and to reduce trapped bubbles. Each layer was then coated with more resin, and the sections were



18 November 2024 17:43:29

FIG. 3. (a) Procedure for fabricating a structured acrylic-GS20 composite. (I) The solid acrylic disk is fabricated to have an alternating odd-even array of blind holes, GS20 cubes are placed into the blind holes, (II) the top of the acrylic disk is covered with PMMA resin, a secondary acrylic disk with a structured array of blind holes is placed on top of the filled acrylic disks, and (III) the process is repeated to the desired length and sealed with a solid acrylic disk with no blind holes; here, the final composite assembly is cured with a UV lamp and diamond turned to remove cured-resin residue on the lateral surface. (b) The final structured composite prototype; here, the irregularly shaped features in the composite are small voids, created during the fabrication process, that scatter the visible light.

then stacked upon one another. A final solid disk, with no bored features, was added to the top [see Fig. 3(a-III)] to act as a cap for the complete stack. Care was taken while stacking to align each layer both horizontally and rotationally. The fully stacked composite assembly was then cured with a UV lamp, and the surfaces were diamond turned with a lathe equipped with an air-bearing spindle to remove the excess material and to achieve a 4.6 cm diameter and 5.08 cm length of the final composite cylinder. While the construction of this composite was completed by hand, previous work has demonstrated a potential pathway forward toward rapid manufacturing using automated techniques.⁸

C. Radiation detection measurements

Two radiation exposure approaches were used: (1) small activity button sources (^{252}Cf , ^{60}Co , ^{232}Th) to compare to the MCNP6 modeling results for gamma and neutron transport and (2) a NIST-traceable ^{252}Cf source to explore high dynamic range capability. In both approaches, the contributions from scattered neutrons at the detector location were not measured. Notably, ^{232}Th was chosen as a surrogate for ^{208}Tl ; here, due to nuclear decay processes in ^{232}Th , a finite fraction of ^{208}Tl exists in ^{232}Th , providing the necessary 2.614 MeV gamma-ray emission. The sample composite had the same dimensions as the simulated composite. The scintillation response characteristics of the composites were measured with the composites coupled to a 7.62 cm diameter Hamamatsu R10133 PMT, equipped with a passive voltage divider, operating at 940 V. A 51 mm diameter EJ-560 silicone pad (Eljen Technology, Sweetwater, TX) was used to optically couple the composite to the PMT window, and the composite was centered on the PMT window. An aluminum enclosure was used to shield the composite

from ambient light and to allow neutrons to impinge on the composite. A specular reflector film (3M Vikuiti™ enhanced specular reflector, ESR) was used to surround the internal lateral and top surface of the aluminum enclosure; this approach ensured a finite air gap between the lateral surface of the composite and specular reflector.¹⁸ The entire system was placed in a dark black enclosure to shield the system from stray light. To enable the dual-readout scheme, the R10133 PMT was modified to measure the count rate (from the seventh dynode) and photo-current (from the anode) simultaneously. Pulse-height spectra were recorded by conditioning the output of the seventh dynode with an in-house charge-sensitive pre-amplifier with a sensitivity of 10 mV/pC and a decay constant of 200 μs , followed by an Ortec 672 spectroscopy shaping amplifier (model #2024) with a shaping time of 0.5 μs and processed by an Ortec 927 ASPEC multi-channel analyzer (MCA). Additionally, the anode current was measured with a Keithley 6485 picoammeter. A NIST-traceable ^{252}Cf source, located at LANL's NFIA facility, produced a variable calibrated neutron flux incident on the detector by using a linear displacement system that enabled adjustments of the detector solid angle. The neutron emission rate of the ^{252}Cf source was 5.35×10^8 neutrons per second into 4π , and the contribution of incident neutrons at the detector location was verified by an MCNP6 model of the NFIA facility. The average gamma emission rate was estimated to be on the order of 10^9 gammas per second.^{19,20}

III. RESULTS AND DISCUSSION

A. MCNP6 simulations—Neutron capture time

The neutron moderation process consists of multiple elastic collision events with the composite constituents (primarily hydrogen in

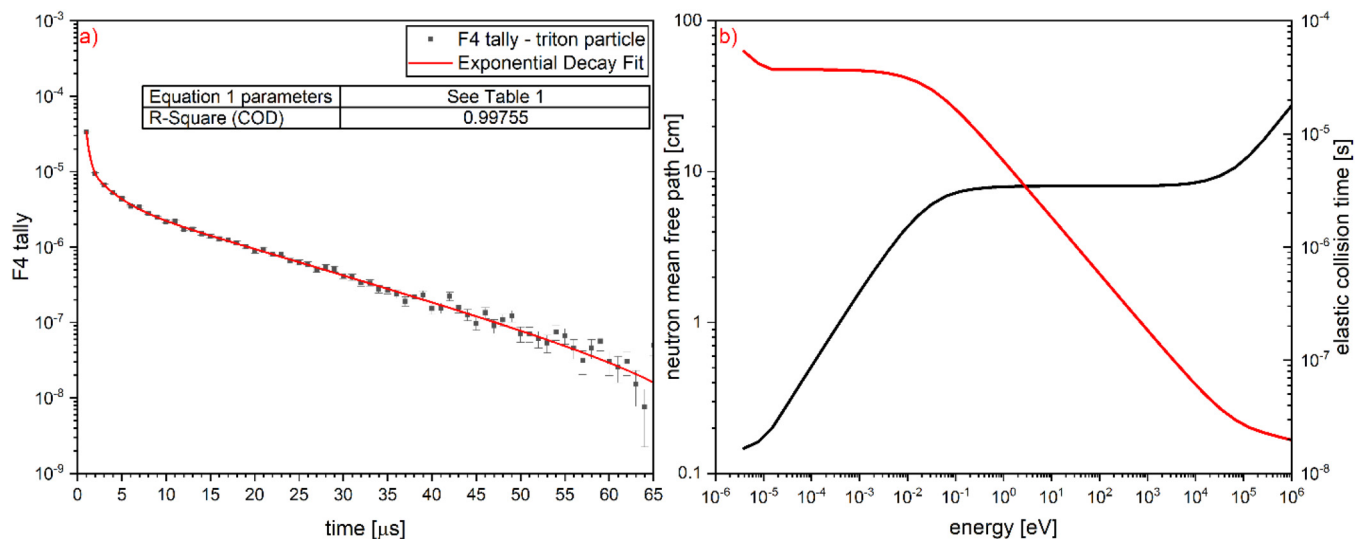


FIG. 4. (a) MCNP6 result for neutron capture time with exposure to ^{252}Cf fission neutrons. The neutron capture time was extracted from the F4 time-tally monitoring the triton particle tracks in the GS20 scintillating particle volume; here, within the first 12 μs , 98.1% of ^{252}Cf fission neutrons, interacting within the composite volume, can be captured. The neutron capture dynamics consists of a fast component with a time constant of $\sim 0.32 \mu\text{s}$ and two slower components with time constants of 2.3 and 12.6 μs , respectively. (b) Neutron mean free path (black trace) and elastic collision time (red trace) as a function of neutron energy in acrylic.

18 November 2024 17:43:29

TABLE I. Least squares fit parameters for Eq. (1) on the F4 time-tally results.

Fit parameter	Parameter value
γ_0	$-1.097 \times 10^{-8} \pm 5.145 \times 10^{-9}$
x_0	1 ± 0
A_1	$2.226 \times 10^{-5} \pm 9.783 \times 10^{-7}$
τ_1	0.319 ± 0.045
A_2	$7.057 \times 10^{-6} \pm 8.084 \times 10^{-7}$
τ_2	2.292 ± 0.264
A_3	$4.292 \times 10^{-6} \pm 1.893 \times 10^{-7}$
τ_3	12.632 ± 0.347

the acrylic moderator), effectively reducing the neutron’s kinetic energy and, thus, increasing the probability of neutron capture by the ${}^6\text{Li}$ isotope in the GS20 scintillator. The neutron kinetic energy directly affects the neutron mean free path and the collision time in the moderator material, which, in turn, governs detector time response; here, as the neutrons elastically scatter in the moderator, the subsequent collision time increases in the moderator. For clarity, the neutron mean free path is the average distance a neutron travels before undergoing an elastic collision event. Figure 4 displays the results for the MCNP6 simulations for neutron capture time together with the macroscopic mean free path for elastic collisions and collision times in acrylic as a function of neutron energy. The results of the least squares fit, for Eq. (1), are displayed in Table I.

Neutron capture time simulations can be used to explore the time response of the neutron capture event for fission neutrons with SPCs. The MCNP6 simulation approach is described in Sec. II A 1.

Because a fission neutron energy distribution can span many orders of magnitude, materials designed to detect energetic neutrons via thermal neutron capture require the ability to accommodate many different neutron mean free paths in the moderator (i.e., acrylic). Because the most probable neutron energy for ${}^{252}\text{Cf}$ fission neutrons is 0.7 MeV, multiple elastic collision events can occur within a fraction of a micro-second.²¹

The three time components extracted from the exponential fit are attributed to neutron energy-dependent moderation, which spans multiple interaction time scales (i.e., 0.1-10’s μs), followed by neutron capture. While no physical interaction can be attributed to each time component, the longest time component provides a timing constraint for neutron counting conventions.

B. MCNP6 simulations—Neutron capture efficiency, gamma rejection ratio, and pulse-height distribution

The neutron capture efficiency of the SPC was determined by calculating the ratio between the total number of ${}^6\text{Li}(n,\alpha){}^3\text{H}$ reactions within the GS20 scintillating cubes and the total number of incident neutrons. For reference, it was found to be 0.261% for a pure ${}^{252}\text{Cf}$ fission neutron spectrum. The gamma rejection ratio was calculated for various gamma energy distributions (i.e., pure ${}^{252}\text{Cf}$ fission gammas, ${}^{60}\text{Co}$, and ${}^{208}\text{Tl}$). A neutron event threshold of 5σ below the neutron capture peak was then set to evaluate the gamma rejection ratio. That is, gamma events that deposited an energy greater than this threshold were considered being misidentified as neutrons. The rejection ratio for ${}^{252}\text{Cf}$ fission gammas, ${}^{60}\text{Co}$, and ${}^{208}\text{Tl}$ were calculated to be 9.8×10^{-7} , 1.4×10^{-6} , and 3.84×10^{-5} , respectively. While the MCNP results for the gamma

18 November 2024 17:43:29

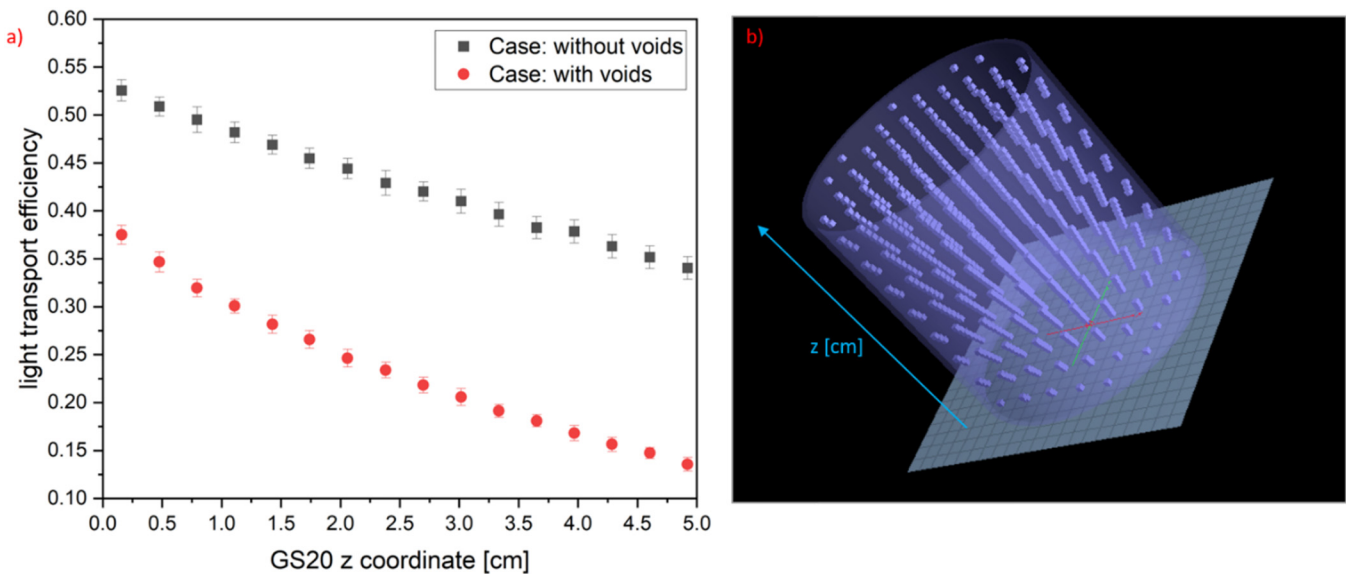


FIG. 5. (a) Average light transport efficiency, together with the standard deviation, as a function of scintillation particle z coordinate for a composite without air voids and for a composite with air voids. (b) FRED rendering of the structured, scintillating particle composite prototype, and z-axis definition; here, the z axis is normal to the PMT detector plane and highlighted in blue font. The solid, square features are the GS20 cubes dispersed in the cylindrical SUVT acrylic matrix.

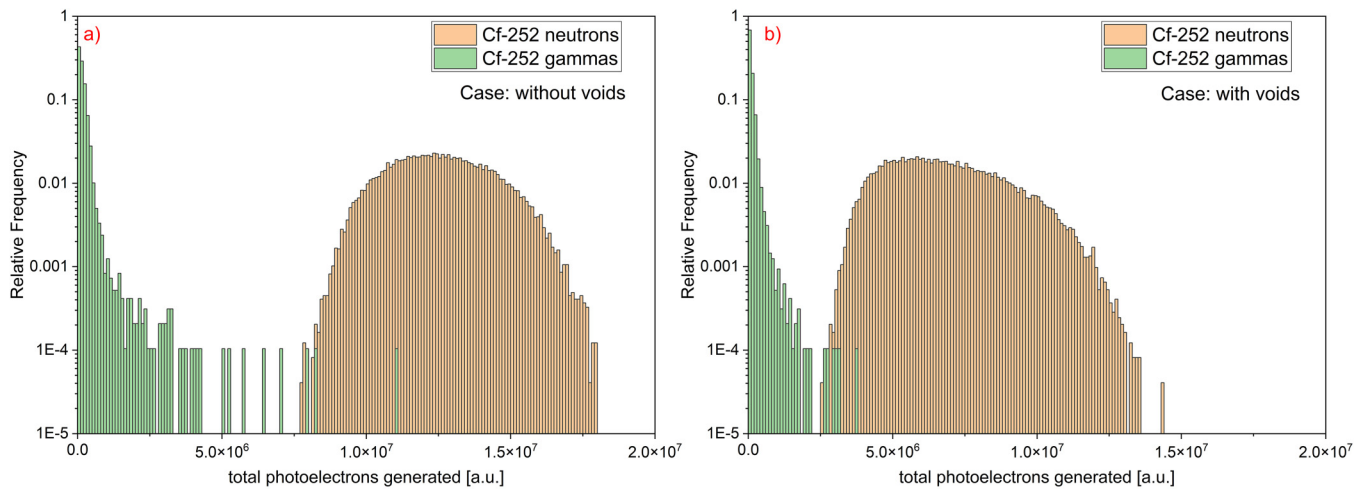


FIG. 6. Simulated total photoelectrons generated histograms for a structured, scintillating particle composite (a) without air voids and (b) with air voids, exposed to a ^{252}Cf source. The total photoelectrons generated were estimated by multiplying the total number of scintillation photons that arrive at the SPC-PMT interface by the PMT quantum efficiency at the wavelength of the scintillator emission maximum and sampling a Poisson distribution for each dynode, up to the seventh dynode.

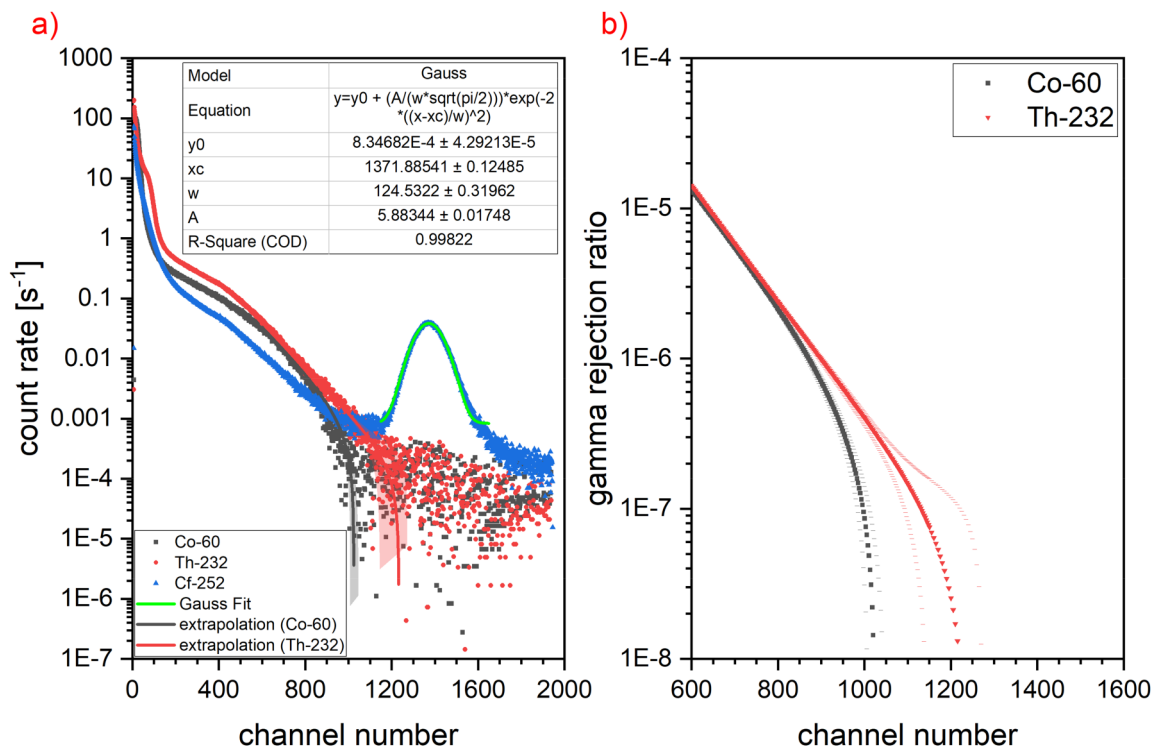


FIG. 7. (a) The background subtracted radiation response results from the small activity button sources (^{252}Cf , ^{60}Co , ^{232}Th) and Gaussian fitting result for the neutron capture peak. Notably, in the region of interest (ROI), between channel numbers 1100 and 1600, significant statistical noise affects the ^{60}Co and ^{232}Th count rate trend. To mitigate this effect, a simple double exponential extrapolation is used to evaluate the gamma rejection ratio. The extrapolation for the ^{60}Co case is shown in the solid black trace, and the extrapolation for the ^{232}Th case is shown in the solid red trace; additionally, the shaded areas represent the three-sigma confidence bands. (b) Gamma rejection ratio for ^{60}Co and ^{232}Th sources as a function of channel number threshold value; here, the dashed lines, above and below the traces, represent the three-sigma confidence bands.

18 November 2024 17:43:29

rejection ratio are quite promising, it is important to emphasize that these results represent a lower bound constraint and are likely higher in practice due to external background contributions. The relatively poor gamma rejection ratio of ^{208}Tl , compared to ^{60}Co , is due to the higher energy of the ^{208}Tl gamma-ray emission compared to the ^{60}Co gamma emission; here, the higher energy enables the ^{208}Tl gamma-ray to undergo multiple interactions (i.e., Compton scattering and pair-production) that collectively produce additional energy deposition events per gamma-ray.

To explore the impact of air voids on light transport efficiency in composites, the average light transport efficiency is shown in Fig. 5.

Figure 5 clearly shows that optical voids can drastically affect the amount of scintillation light collected by a photo-sensitive device (e.g., PMT or SiPM). To look at the impact of optical voids in more detail, the total photoelectrons generated histograms were calculated for each case (Fig. 6). This calculation used the spatial locations of the $^6\text{Li}(n,\alpha)^3\text{H}$ nuclear reactions and energetic electron events previously determined by MCNP6 simulations. For each $^6\text{Li}(n,\alpha)^3\text{H}$ event or energetic electron event, the total number of photons reaching the PMT-SPC interface was calculated and tabulated to generate a photon histogram. An approximate total photoelectrons generated histogram was then created by the method described in experimental details (see Sec. III A). Figure 6 displays

the pulse-height distribution simulation results comparing a composite with air voids with a composite without air voids for various sources.

As shown in Fig. 6(a), the SPC without air voids shows a localized Gaussian distribution for ^{252}Cf neutron capture events (at $\sim 1.25 \times 10^7$ electrons), with the ^{252}Cf gamma events only minimally overlapping with the ^{252}Cf neutron capture distribution. On the other hand, the air-void case shown in Fig. 6(b) shows a broader neutron capture event distribution and, thus, a relatively greater ^{252}Cf gamma event overlap. The result of these two distinct cases shows that optical voids can degrade the gamma rejection ratio, reduce scintillation light collection at the PMT interface, and broaden the neutron capture event distribution.

C. Pulse-height distribution measurements

Figure 7 displays the results for the small activity button sources (^{252}Cf , ^{60}Co , ^{232}Th). In Fig. 7(a), the response to incident neutrons from ^{252}Cf produces a localized Gaussian distribution, centered near channel number 1372, with a full width at half maximum (FWHM) of 10.7%. Additionally, the localized Gaussian distribution sits above a small gamma continuum that is likely due to gamma emission from ^{252}Cf and other associated isotopes in the nuclear decay process.

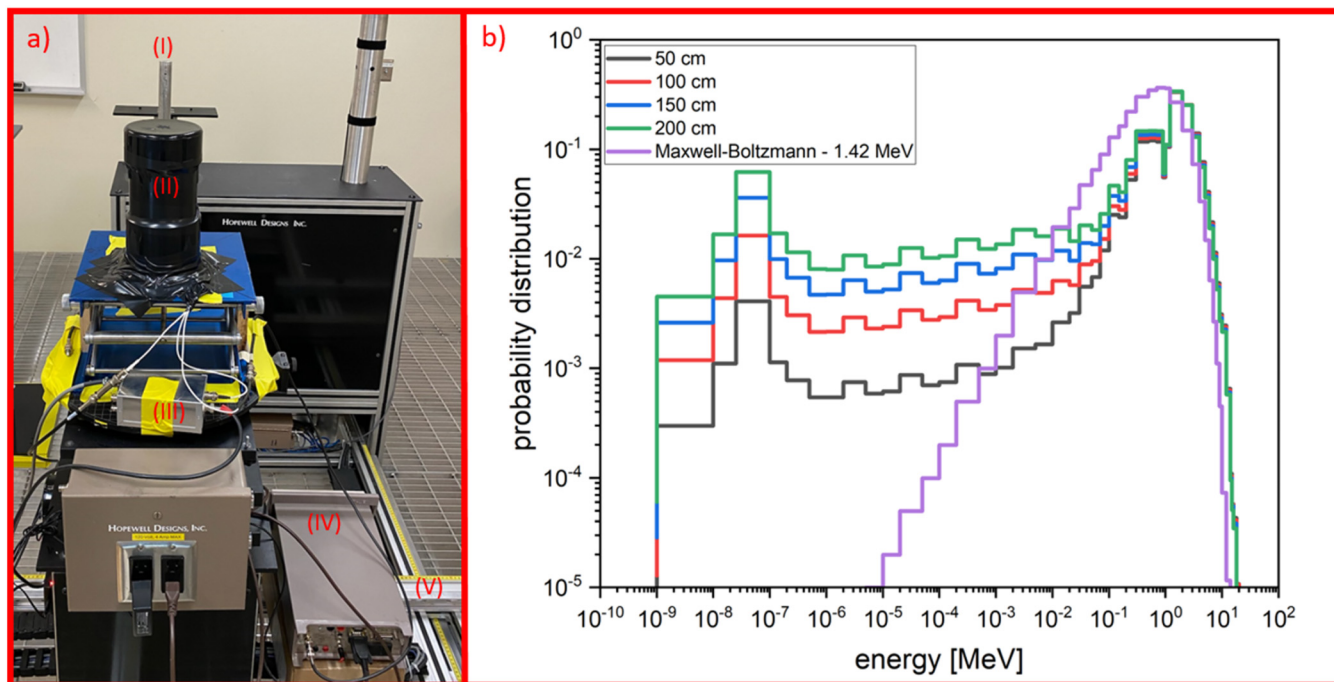


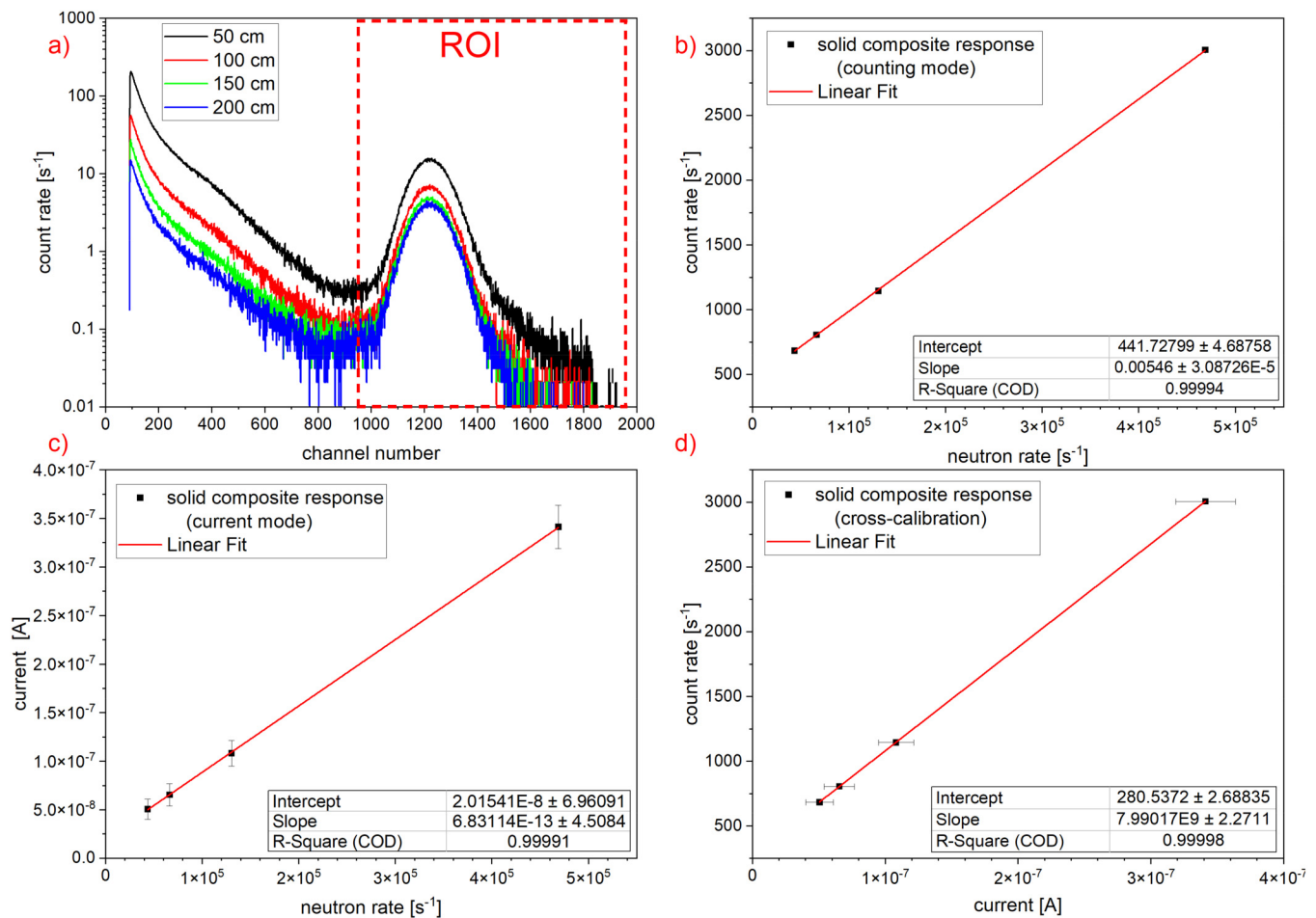
FIG. 8. (a) The experimental setup at the NFIA facility; here, the roman numerals in the red font highlight the major components in this experiment: (I) ^{252}Cf source, (II) composite detector and corresponding dark, black enclosure, (III) pre-amplifier conditioning output from the seventh dynode, (IV) Keithley 6485 pico-ammeter for current measurements, and (V) linear displacement system used to adjust detector alignment and incident neutron fluence. (b) MCNP6 results for the NIST-traceable ^{252}Cf source; the neutron source probability distribution for different distances from the ^{252}Cf source at the NFIA facility along with the theoretical source probability distribution assuming a temperature of 1.42 MeV. The neutron source probability for the NFIA facility is the area normalized F5 tally results.

18 November 2024 17:43:29

The FWHM of the neutron capture peak distribution, compared to 15% obtained from previous efforts,⁶ strongly suggests that light transport is significantly improved by the acrylic disk stacking approach using acrylic resin. Figure 7(b) displays the gamma rejection ratio as a function of channel number threshold. In the neutron capture peak regime, between channel numbers 1100–1600, the gamma rejection ratio can be on the order of 10^{-7} or less, depending on the channel number threshold value. Remarkably, in Fig. 7(b), we can also show good agreement with the calculated MCNP6 results for the ^{60}Co source case; here, the gamma rejection ratio for the ^{60}Co source case is 3.8×10^{-6} at channel number 750, which represents 5σ away from the Gaussian centroid around channel number 1372. (See Sec. III B) This result demonstrates good gamma insensitivity in different, high-energy gamma background environments while operating in counting mode.

Figure 8 displays the experimental setup at the NFIA facility and the MCNP6 results for the NIST-traceable ^{252}Cf source distribution at the NFIA facility. Figure 8(b) clearly demonstrates that as the distance of the detector from the source is increased, the relative fraction of scattered neutron contributions increases significantly. The likely source of this scattered neutron contribution arises from the thick concrete walls present in the facility and surrounding equipment used in the measurement; additionally, the low-energy neutron contribution also creates delayed gamma rays through activation processes. Figure 8(b) also highlights the differences between the incident neutron distributions at the NFIA facility compared to a pure ^{252}Cf source, assuming a Maxwell-Boltzmann distribution with a temperature of 1.42 MeV.

Using the NIST-traceable ^{252}Cf source, together with the MCNP6 results describing the incident neutron fluence at the NFIA



18 November 2024 17:43:29

FIG. 9. (a) Representative, background subtracted, pulse-height spectra taken with the detector at 50, 100, 150, and 200 cm from the calibrated NFIA ^{252}Cf source. The region of interest (ROI) defines the integration interval used to determine the total number of neutron capture events during the measurement. (b) ROI count rate as a function of incident neutron rate; here, the count rate was determined by the total number of events in the ROI normalized by the acquisition time, and the data were taken with the detector at different distances from the calibrated NFIA source. (c) Measured PMT current as a function of incident neutron rate; similarly, the data were taken with the detector at different distances from the calibrated NFIA source. (d) Count rate vs current correlation plot; here, the inverse of the slope of this line represents the average charge produced by the PMT per neutron capture event.

facility, we explored the response of the detector in both the counting mode and current mode. Figure 9 displays the results of the detector operating in the counting mode and current mode simultaneously while being exposed to the NIST-traceable ^{252}Cf neutron source.

As expected, Fig. 9(a) demonstrates a similar ^{252}Cf neutron source response as Fig. 7(a); however, one notable difference is the centroid value at channel number 1221 vs channel number 1372 in Fig. 7(a), which is due to shaping amplifier fine gain adjustments performed prior to the measurements at the NFIA facility. In Fig. 9(b), two key observations are made. First, the y-intercept does not cross through the origin; this is attributed to gamma rays created through delayed activation in the NFIA facility. Second, the slope of the linear fit represents the average overall neutron detection efficiency at the NFIA facility, which was found to be $0.546 \pm 0.003\%$. Notably, this value is higher than the calculated intrinsic neutron detection efficiency of 0.261% (see Sec. III B). The difference between the experimental result and the MCNP6 result, modeling a pure ^{252}Cf source, is directly due to the scattered neutron contributions; here, scattered neutrons (<1 MeV) have a higher probability of being detected compared to fast neutrons (≥ 1 MeV). For direct comparison, Table II displays the overall neutron detection efficiency at the NFIA facility as a function of distance, extracted from the NFIA experiment, compared to the MCNP6 results. Like the count rate [Fig. 9(b)], the current output [Fig. 9(c)] scaled linearly with incident neutron rate, reinforcing that this multi-signature response can support a cross-calibration between the count rate and average current. The inverse of the slope of the line in Fig. 9(d) represents the average PMT charge output per neutron capture event, and a value of 125 pC per neutron capture event was found. The average PMT charge output per neutron capture event represents a cross-calibration constant that allows us to convert the PMT current to a corresponding neutron detection rate. Based on the results, and taking into account that the maximum average current for the R10133 PMT is $100\ \mu\text{A}$, this would enable a linear response of up to a maximum detector count rate of 8×10^5 cps, using the cross-calibration constant, in the current mode in this experiment. Notably, even higher maximum count rates could be achieved by lowering the PMT operating voltage to adjust the PMT gain or by using a PMT with a higher maximum current rating.

TABLE II. Experimental overall neutron detection efficiency at the NFIA facility as a function of distance compared to the MCNP6 result assuming a Maxwell–Boltzmann distribution [see Fig. 8(b)]. The experimental overall neutron detection efficiency at the NFIA facility was calculated by integrating the total number of counts in the ROI and normalizing by the acquisition time, followed by dividing by the incident neutron rate determined by MCNP6 calculations.

Detector to ^{252}Cf source distance (cm)	Overall efficiency (%)	Intrinsic efficiency (%)
	NFIA experiment	MCNP results
50	0.641 ± 0.195	0.436
100	0.877 ± 0.305	0.79
150	1.214 ± 0.359	1.28
200	1.564 ± 0.390	1.81
Maxwell–Boltzmann	N/A	0.261

Compared to the MCNP6 results, the experimental overall neutron detection efficiency values obtained for the detector at various distances from the source agree fairly well. Because cadmium shielding was not implemented during this experiment, distance-dependent contributions of scattered neutrons increased the value of the overall neutron detection efficiency derived from the measurements [see Fig. 8(b)]. The main source of uncertainty, for the overall efficiency measurement, originates from statistical considerations of the total number of neutrons counted. Due to experimental time constraints, the exact neutron scattering contributions from surrounding equipment, using exact positions, could not be taken into account. However, these results allow us to constrain the neutron detection efficiency and demonstrate good agreement between the experiment and simulation results. Using the average overall neutron detection efficiency from Fig. 9, the maximum count rate corresponds to a maximum incident neutron rate of 1.47×10^8 neutrons per second. If one considers the $23.368\ \text{cm}^2$ surface area (length \times diameter), the maximum incident neutron flux that can be handled by the composite detector is $6.29 \times 10^6\ \text{cm}^{-2}\text{s}^{-1}$. While this numerical exercise represents the limitation of the cross-calibration approach, this limitation could be improved by, for example, reducing the scintillating particle volume fraction, using a PMT with a higher maximum current rating or by tuning the gain of the PMT.

IV. CONCLUSIONS

We have demonstrated for the first time that solid, structured scintillating particle composites (SPCs) offer fast neutron capture times and provide a linear response to a high flux of incident fission neutrons from a ^{252}Cf neutron source. By using a novel cross-calibration method, we have enabled a new technique for operation in mixed neutron–gamma environments that provides quantitative neutron flux information, up to an incident neutron flux of $6.29 \times 10^6\ \text{cm}^{-2}\text{s}^{-1}$ in the present detector configuration. We also demonstrated a scalable fabrication technique for solid, structured SPCs that possess small optical voids. Coupled MCNP6-FRED simulations elucidated the role of small optical voids on scintillation light collection and the gamma rejection ratio, indicating that reducing the optical void content can improve neutron detection performance in future design iterations. The overall neutron detection efficiency, for a ^{252}Cf neutron source, was found to be $0.546 \pm 0.003\%$, in good agreement with the MCNP6 simulation results. The small discrepancies between the experimental and MCNP6 simulation results are attributed to environmental effects not taken into account. In conclusion, SPCs can enable high performance neutron detector solutions for a variety of applications that require large active volumes or detecting neutrons over large dynamic ranges.

ACKNOWLEDGMENTS

Research presented in this article was supported by the Laboratory Directed Research and Development program of Los Alamos National Laboratory under Project No. 20210431ER. This work was supported by the National Nuclear Security Administration, Defense Nuclear Nonproliferation Directorate, Office of Nonproliferation Research and Development.

AUTHOR DECLARATIONS

Conflict of Interest

The authors have no conflicts to disclose.

Author Contributions

Brenden W. Wiggins: Conceptualization (equal); Formal analysis (equal); Funding acquisition (supporting); Investigation (equal); Methodology (equal); Project administration (supporting); Resources (equal); Supervision (equal); Validation (equal); Writing – original draft (lead); Writing – review & editing (equal). **Cameron G. Richards:** Data curation (equal); Investigation (equal); Visualization (equal); Writing – review & editing (equal). **Thomas D. McLean:** Data curation (equal); Resources (equal); Validation (equal); Writing – review & editing (equal). **Metodi Iliev:** Data curation (equal); Investigation (equal); Methodology (equal); Writing – review & editing (equal). **Andrea Favalli:** Investigation (equal); Methodology (equal); Supervision (equal); Writing – review & editing (equal). **Markus P. Hehlen:** Conceptualization (equal); Funding acquisition (equal); Investigation (equal); Project administration (equal); Supervision (equal); Writing – review & editing (equal).

DATA AVAILABILITY

The data that support the findings of this study are available from the corresponding author upon reasonable request.

REFERENCES

- ¹A. Favalli, B. W. Wiggins, C. G. Richards, K. Ogren, T. D. McLean, K. D. Ianakiev, and M. P. Hehlen, "Next-generation neutron detection using a ⁶Li glass scintillator composite," Commun. Phys. (unpublished).
- ²G. F. Knoll, *Radiation Detection and Measurement* (John Wiley & Sons, Inc., Ann Arbor, Michigan, 2012).
- ³K. Kazkaz, N. S. Bowden, and M. Pedretti, "Comparison of lithium gadolinium borate crystal grains in scintillation and non-scintillating plastic matrices," *IEEE Trans. Nucl. Sci.* **60**, 1416–1426 (2013).
- ⁴M. Mayer, J. Nattress, V. Kukharev, A. Foster, A. Meddeb, C. Trivelpiece, Z. Ounaies, and I. Jovanovic, "Development and characterization of a neutron detector based on a lithium glass-polymer composite," *Nucl. Instrum. Methods Phys. Res. A* **785**, 117–122 (2015).
- ⁵G. C. Rich, K. Kazkaz, H. P. Martinez, and T. Gushue, "Fabrication and characterization of a lithium glass-based composite neutron detector," *Nucl. Instrum. Methods Phys. Res. A* **794**, 15–24 (2015).
- ⁶K. D. Ianakiev, M. P. Hehlen, M. T. Swinhoe, A. Favalli, M. L. Iliev, T. C. Lin, B. L. Bennett, and M. T. Barker, "Neutron detector based on particles of ⁶Li glass scintillator dispersed in organic light guide matrix," *Nucl. Instrum. Methods Phys. Res., Sect. A* **784**, 189–193 (2015).
- ⁷B. Wiggins, A. Favalli, M. L. Iliev, K. D. Ianakiev, and M. P. Hehlen, "Computational investigations of arranged scintillating particle composites for fast neutron detection," *Nucl. Instrum. Methods Phys. Res., Sect. A* **915**, 17–23 (2019).
- ⁸B. W. Wiggins, M. L. Iliev, A. Favalli, K. D. Ianakiev, and M. P. Hehlen, "Developments in additive manufacturing of arranged scintillating particle composites for neutron detection" *Proc. SPIE* 10762, 107620F (2018).
- ⁹C. G. Richards, B. W. Wiggins, M. Iliev, A. Favalli, T. D. McLean, A. Gomez, and M. P. Hehlen, "Performance assessment of a compact neutron detector module based on scintillating composites," *SPIE* **12241**, 122410A (2022).
- ¹⁰M. J. Cieślak, K. A. A. Gamage, and R. Glover, "Critical review of scintillating crystals for neutron detection," *Crystals* **9**, 480 (2019).
- ¹¹B. Wiggins, C. G. Richards, R. O. Nelson, M. Iliev, and M. Hehlen, "Investigations of radiation damaged arranged scintillating particle composites," *J. Appl. Phys.* **130**, 193102 (2021).
- ¹²A. Favalli *et al.*, "Pulse shape discrimination properties of neutron-sensitive organic scintillators," *IEEE Trans. Nucl. Sci.* **60**, 1053–1056 (2013).
- ¹³E. P. Shabalin, *Fast Pulsed and Burst Reactors* (Pergamon, 2013), ISBN-10:1483172597.
- ¹⁴M. B. Chadwick, M. Herman, P. Oblozinsky *et al.*, "ENDF/B-VII.1 nuclear data for science and technology: Cross sections, covariances, fission product yields and decay data," *Nucl. Data Sheets* **112**(12), 2887–2996 (2011).
- ¹⁵"MCNP Users Manual—Code Version 6.2," Los Alamos National Laboratory, report LA-UR-17-29981, edited by C. J. Werner (2017).
- ¹⁶International Organization for Standardization, "Reference neutron radiations—Part 2: Calibration fundamentals of radiation protection devices related to the basic quantities characterizing the radiation field," in *ISO 8529-2:2000* (International Organization for Standardization, Geneva, 2000).
- ¹⁷A. W. Dalton, "Light conversion efficiency of small lithium scintillators for electrons, protons, deuterons and alpha particles," *Nucl. Instrum. Methods Phys. Res., Sect. A* **254**, 361–366 (1987).
- ¹⁸M. P. Hehlen *et al.*, "Light propagation in a neutron detector based on ⁶Li glass scintillator particles in an organic matrix," *J. Appl. Phys.* **124**, 124502 (2018).
- ¹⁹A. B. Smith, P. R. Fields, and A. M. Friedman, "Prompt gamma rays accompanying the spontaneous fission of Cf²⁵²," *Phys. Rev.* **104**(3), 699–702 (1956).
- ²⁰E. J. Axton and A. G. Bardell, "Neutron yield from the spontaneous fission of ²⁵²Cf ($\bar{\nu}$)," *Metrologia* **21**(2), 59–74 (1985).
- ²¹R. C. Martin, J. B. Knauer, and P. A. Balo, "Production, distribution and applications of californium-252 neutron sources," *Appl. Radiat. Isot.* **53**, 785–792 (2000).